



# Facile manipulation of mechanical properties of Ti-6Al-4V through composition tailoring in laser powder bed fusion



Xi Du <sup>a,b</sup>, Marco Simonelli <sup>a</sup>, James W. Murray <sup>b</sup>, Adam T. Clare <sup>b,c,\*</sup>

<sup>a</sup> Centre for Additive Manufacturing, Faculty of Engineering, The University of Nottingham, Nottingham NG8 1BB, UK

<sup>b</sup> Advanced Component Engineering Laboratory (ACEL), Faculty of Engineering, University of Nottingham, Nottingham NG7 2RD, UK

<sup>c</sup> Department of Mechanical Engineering, University of British Columbia, Vancouver Campus, 6250 Applied Science Lane, Vancouver, Canada

## ARTICLE INFO

### Article history:

Received 22 September 2022

Received in revised form 5 January 2023

Accepted 22 January 2023

Available online 23 January 2023

### Keywords:

Laser powder bed fusion

Ti-6Al-4V

Composition tailoring

In-situ alloying

Mechanical properties

## ABSTRACT

Ti-6Al-4 V alloy when processed by laser powder bed fusion (LPBF) is a useful material which can be used for the manufacture of complex 3D components for aerospace and medical applications. LPBF fabricated Ti-6Al-4 V typically shows high tensile strength (> 1200 MPa) but poor ductility (< 10%), explained by the characteristic microstructures that form under high cooling rates and multiple thermal cycles. Here, the composition of the feedstock Ti-6Al-4 V powder was modified via the addition of commercially pure Ti (CP Ti) to achieve improved ductility of LPBF parts through an in-situ modified composition, while maintaining good strength. The LPBF printed Ti alloy (with nominal composition Ti-3Al-2 V) showed a tensile strength of ~1000 MPa, with improved ductility (~13%), comparable to wrought Ti-6Al-4 V. These properties are thought to be explained by the decreased c/a ratio (where c and a are the lattice parameters of the titanium hexagonal close-packed phase) resulting in enhanced dislocation slip. Good relative density was also achieved using the modified composition under the same processing parameters. Some non-uniform regions were seen in the developed alloys, as well as evidence of increased martensite  $\alpha'$  thickness. It is proposed that with optimized parameters, further enhancements may be achieved. This work has shown that microstructural and mechanical properties can be readily manipulated with proper CP Ti addition.

© 2023 The Author(s). Published by Elsevier B.V. This is an open access article under the CC BY license (<http://creativecommons.org/licenses/by/4.0/>).

## 1. Introduction

The Additive manufacturing (AM) sector is growing rapidly due to its ability to produce complex shaped 3D parts from digital models [1]. Laser powder bed fusion (LPBF, also often referred to as selective laser melting) is a key AM process to produce complex shaped metallic parts including steels [2,3], titanium and its alloys [4,5], aluminum alloys [6,7] and Ni-based superalloys [8,9], useful across a range of industries. Ti based alloys with high strength-to-weight ratio, good biocompatibility, and high corrosion resistance, are of particular interest to the AM community, given their use for aerospace and medical applications [10–13].

LPBF fabricated Ti-6Al-4 V alloy usually presents columnar prior- $\beta$  grain boundaries with an acicular martensite  $\alpha'$  structure. This is explained by high temperature gradient and high cooling rates during cyclic heating and cooling during the LPBF process [11,13]. As a result, the mechanical properties of LPBF built Ti-6Al-4 V typically

show high tensile (1200 MPa) and yield strength but poor ductility (less than 10%) [11,13–15]. Components built in this fashion also exhibit anisotropic properties.

A common solution to improve ductility (to beyond 10%) is to heat-treat in a furnace to decompose the acicular martensite  $\alpha'$  structure into  $\alpha$  and  $\beta$  phases. There is a significant body of work in the literature based on heat treatment of LPBF Ti-6Al-4 V alloys to balance the strength and ductility [16–20]. For example, Vrancken et al. [16] reported an increased ductility of LPBF printed Ti-6Al-4 V alloy from 7.28% to 12.84% via heat treatment, with a decreased tensile strength from 1267 MPa to 1004 MPa. Ju et al. [17] and Zhang et al. [18] also achieved enhanced ductility with reduced strength by appropriate heat treatment. It is noteworthy that Zou et al. [19] also achieved high ductility (increased from 5.2% for as-built to 16.6%), partially explained by refined prior- $\beta$  grains of Ti-6Al-4 V after rapid heat treatment.

Heat treatment processes with Argon or in a vacuum can be costly, time-consuming, energy-consuming, and may not always be available. The brittleness of as-built Ti-6Al-4 V alloys by LPBF may cause build failure by cracking or delamination of the parts that cannot accommodate thermal stresses created during the process via plastic deformation [1,13]. There is therefore a great interest in

\* Corresponding author at: Advanced Component Engineering Laboratory (ACEL), Faculty of Engineering, University of Nottingham, Nottingham NG7 2RD, UK.

E-mail address: [adam.clare@nottingham.ac.uk](mailto:adam.clare@nottingham.ac.uk) (A.T. Clare).

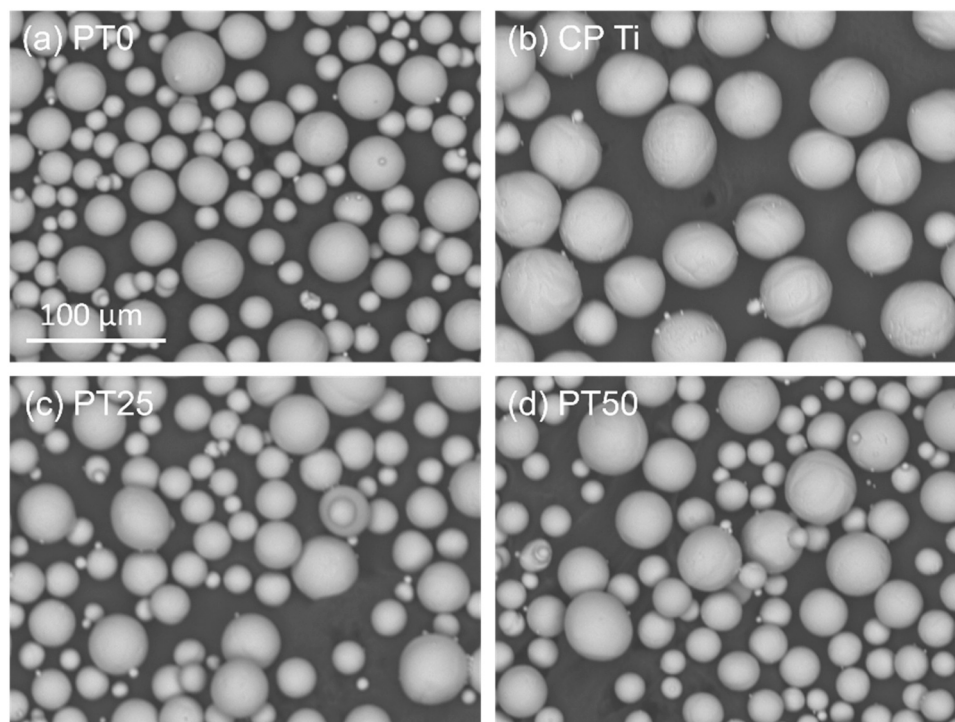


Fig. 1. SEM images of powder feedstock (a) PT0, (b) CP Ti, (c) PT25, and (d) PT50.

achieving balanced strength-ductility properties in Ti-6Al-4 V without a post-processing step. Process parameters optimization can go some way to achieve this. For example, Xu et al. [21,22] produced LPBF Ti-6Al-4 V with a tensile strength of 1150 MPa and ductility around 11%, via in-situ decomposition of martensite  $\alpha'$  into  $\alpha$  and  $\beta$  (in a similar process to heat-treatment) through careful optimization of processing parameters (in particular focal offset distance). This implies that the temperature profile can be controlled to achieve in-situ decomposition of martensite  $\alpha'$  with a proper combination of the key processing parameters. Liu et al. [23] also reported high strength and improved ductility ( $\sim 1200$  MPa and  $\sim 10\%$  respectively) of as-built Ti-6Al-4 V by LPBF with more  $\alpha$  phase than martensite  $\alpha'$  after processing parameters optimization. Although ductility can be enhanced through adjusting processing parameters, the optimized parameters may not be practical or may result in other properties undesirable to the part, like surface roughness. In addition, the maximum ductility achievable might be limited. Also tuning of in-situ heat treatment might not be possible for a geometry where the cross section varies significantly through the build height.

Due to the high strength (over 1200 MPa) of the martensite  $\alpha'$  structure in as-built parts by LPBF, there is headroom for a somewhat decreased strength in exchange for significantly improved ductility. It is therefore reasonable to consider a more drastic approach of composition modification of the initial feedstock to achieve a more balanced strength-ductility in LPBF built Ti-6Al-4 V. Recently, Wang et al. [24] used a new pre-alloyed Ti-4Al-4 V powder material to produce LPBF parts with good ductility ( $\sim 13\text{--}14\%$ ) and reduced strength (tensile strength  $\sim 930$  MPa, yield strength  $\sim 830$  MPa). This approach however, which uses a pre-alloyed powder, limits the flexibility to produce a specific composition of powder and therefore a part, with tailored properties. In addition, there is naturally a higher cost associated with a pre-alloyed powder; particularly when the composition is bespoke. For example there are only a handful of pre-alloyed Ti-Al-V based metal powders with modified composition from Ti-6Al-4 V [25,26].

Nevertheless, there is significant space to explore new compositions which sacrifice some strength to achieve improved ductility.

It is known that CP Ti with very low solute content always produces parts with low strength but excellent ductility ( $\sim 20\%$  ductility), including in LPBF parts with martensite  $\alpha'$  structure [4,27]. A practical and low-cost method of producing higher ductility compositions is by the introduction of CP Ti to initial Ti-6Al-4 V feedstocks prior to LPBF. The in-situ composition tailoring approach can also be exploited to obtain desired microstructures difficult to achieve via pre-alloyed powders.

In this work, Ti-6Al-4 V powder was mixed with CP Ti powder to form two specific Ti alloy compositions (nominal Ti-4.5Al-3 V and Ti-3Al-2 V). For reference, the nearest available grades are Ti-4Al-2 V (TA17) alloy and Ti-3Al-2.5 V (Grade 9) respectively. A detailed microstructural characterization study was carried out, along with tensile testing. A comprehensive discussion is included which explains the mechanical properties achieved in reference to the microstructures observed.

## 2. Experimental

### 2.1. Powder preparation

Plasma atomized Ti-6Al-4 V (Grade 23 with oxygen content no more than 0.13 wt%, 15–45  $\mu\text{m}$ ) and spherical CP Ti (Grade 1 with oxygen content no more than 0.18 wt%, 38–63  $\mu\text{m}$ ) were blended using resonant acoustic mixing. Two powders were prepared using addition of CP Ti at 25 wt%, 50 wt% introduced into Ti-6Al-4 V to form nominal Ti-4.5Al-3 V (called PT25,  $D_{50} = 37.7$   $\mu\text{m}$ ), Ti-3Al-2 V (half of Ti-6Al-4 V, called PT50,  $D_{50} = 39.8$   $\mu\text{m}$ ) respectively. The unmodified Ti-6Al-4 V without CP Ti addition is called PT0 ( $D_{50} = 33.7$   $\mu\text{m}$ ) for reference. The powder feedstocks PT0, CP Ti, PT25, and PT50 were observed by scanning electron microscope (Hitachi TM3030), as shown in Fig. 1.

### 2.2. LPBF experiments

For each powder feedstock (PT0, PT25 and PT50), cubic samples with size  $10 \times 10 \times 5$   $\text{mm}^3$  and tensile bars with  $\phi 9 \times 60$  mm were

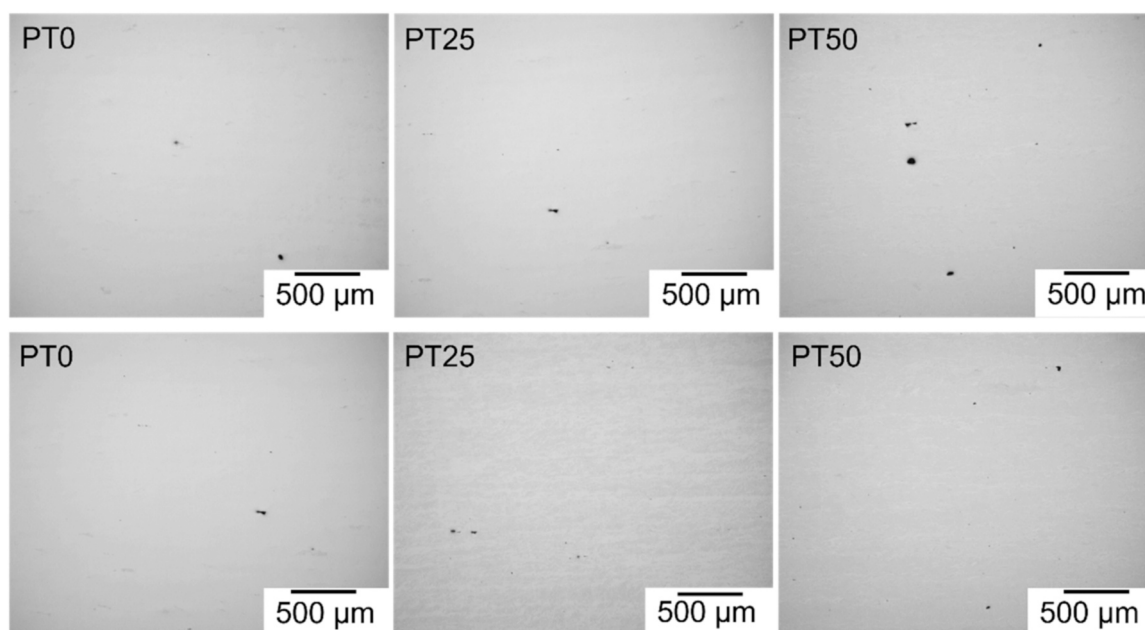


Fig. 2. Optical microscopy images showing porosity (relative density) of as-built PT0, PT25, and PT50.

fabricated using a Renishaw AM400 LPBF machine equipped with a 400 W Yb fiber laser. A reduced build volume (RBV) configuration with build volume  $78 \times 78 \times 55 \text{ mm}^3$  was used to accommodate the small amounts of powder available. Typical processing parameters for Ti-6Al-4V, identified through prior experimentation, were used: power 200 W, point distance  $75 \mu\text{m}$ , exposure time  $50 \mu\text{s}$ , hatch distance  $65 \mu\text{m}$  and layer thickness  $30 \mu\text{m}$ . A standard scanning rotation ( $67^\circ$ ) approach between two consecutive layers was used for all samples.

### 2.3. Materials characterization

As-built cubic samples were sectioned, ground and polished for porosity analysis. The polished samples were further etched using Kroll's reagent to reveal the microstructure. Optical microscopy (OM, Nikon ECLIPSE LV100ND) was used to observe the porosity and etched microstructure for PT0, PT25, and PT50. The porosity of two OM images (each image captured in 5X magnification with the size around  $2.1 \times 2.7 \text{ mm}$ ) for each sample was measured by open source software ImageJ using an automated threshold approach. Phase identification of the polished cubic samples for PT0, PT25, and PT50 was performed using X-ray Diffraction (XRD, Bruker D8 ADVANCE) using Cu K $\alpha$  radiation with 2-theta angles from  $30^\circ$  to  $90^\circ$ . The XRD peak positions (2-theta angle) were calculated using the centroid method [28] using an in-house developed MATLAB script. Peak positions were then used to estimate the lattice parameters and the c/a ratio in the hexagonal close-packed (HCP) phase of titanium. Microstructural and chemical information of all samples were obtained by scanning electron microscopy (SEM) (JEOL-7100 F FEG-SEM) with Energy Dispersive X-Ray Spectroscopy (EDS). EDS was used for elemental distribution analysis with area maps (accelerating voltage 15 kV, magnification 1000X). Martensite  $\alpha'$  thickness in SEM images of printed samples was also measured using three SEM images with high magnification 3000X for each sample and ImageJ with manual measurement (twenty acicular martensite structures were counted and averaged for each SEM image) [29]. Crystallographic analysis was also carried out for printed samples after polishing with colloidal silica using electron backscatter diffraction (EBSD) in the JEOL-7100 F with a step size of  $0.25 \mu\text{m}$ . The collected EBSD data was analysed by software AZtecCrystal and HKL-Channel 5<sup>TM</sup>.

Microhardness data was collected using a digital microhardness tester (Wilson VH3100) with 48 indentations per sample in a  $6 \times 8$  array using 500 gf and a dwell time of 10 s. The as-built tensile bars were mechanically machined into a dog-bone shape with gauge diameter 4 mm and gauge length 20 mm based on ASTM E8/8 M-16a. Tensile tests were then carried out on an Instron 5969 with a displacement rate of 0.14 mm/min at room temperature. A video gauge was used to track and record the strain (elongation) with a high measurement resolution. Two samples were tested for each Ti alloy. The fracture morphology of the tested tensile specimens was observed by SEM (JEOL 6490LV). Fractured PT0 and PT50 after tensile testing were also measured by EBSD to help explain the ductility observed.

## 3. Results

### 3.1. Porosity and homogeneity

Fig. 2 shows representative optical images of polished LPBF printed samples of PT0, PT25, and PT50. PT0 and PT25 showed similar levels of porosity ( $\sim 0.02\%$ , relative density  $\sim 99.98\%$ ). A slight increase in porosity was seen in the PT50 sample ( $\sim 0.07\%$ , relative density  $\sim 99.93\%$ ). Overall, all samples had a good relative density even with the addition of up to 50 wt% CP Ti.

Fig. 3 shows the elemental distribution of Ti, Al, and V in central regions of as-built PT0, PT25, and PT50 samples. Backscattered electron (BSE) images provide a direct qualitative observation of elemental homogeneity. In the case of the PT0 (pre-alloyed Ti-6Al-4V), it is homogenous with no obvious heterogeneities in BSE imaging or in EDS maps (see Fig. 3(a1-a4)). With the addition of CP Ti (PT25 and PT50), notable regions of dark contrast appear in BSE images. EDS area maps show the elemental distribution of Ti, Al, and V. Obviously poor Al areas in PT25 and PT50 corresponding to dark areas in BSE images can be observed. Slightly poor V areas in PT25 and PT50 corresponding to dark areas in BSE images are also presented. These non-uniform areas therefore are most probably Ti rich areas though it is not clearly identified by Ti maps due to the small relative difference between CP Ti and Ti-6Al-4V for Ti element. The average elemental content based on the EDS area maps for PT0, PT25 and PT50 in Fig. 3 is shown in Table 1. It is noteworthy that Al and V

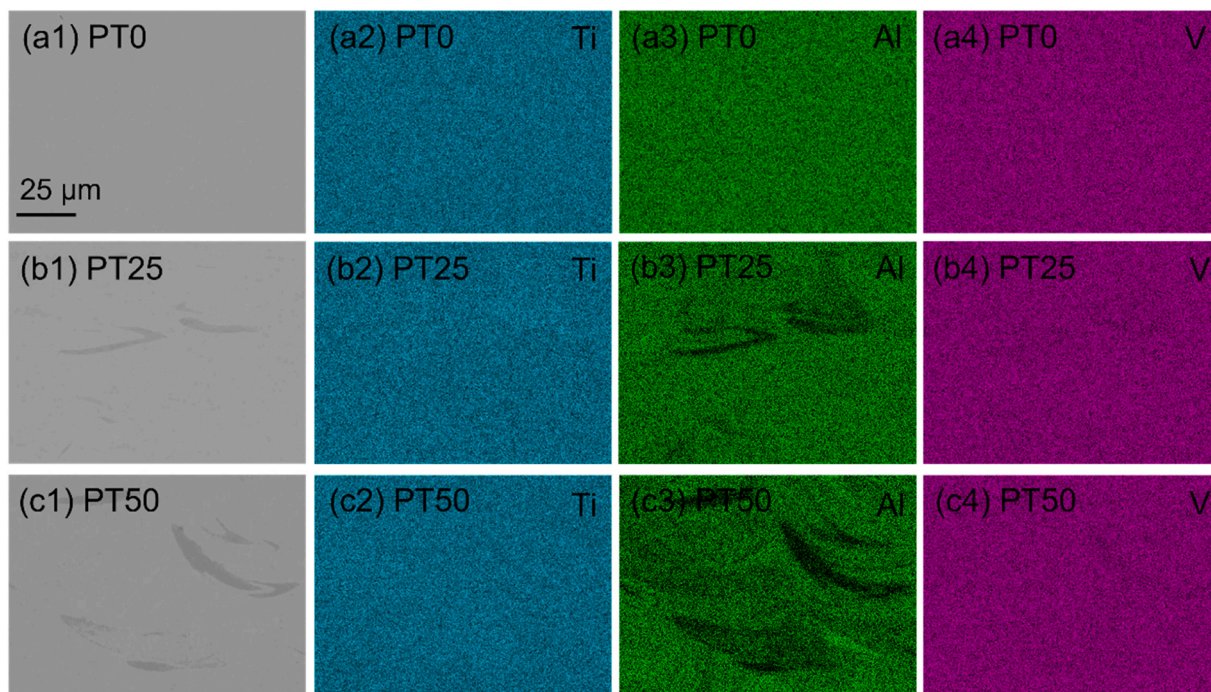


**Fig. 3.** Backscattered electron (BSE) images and EDS area maps of as-built (a1-a4) PT0, (b1-b4) PT25, and (c1-c4) PT50.

**Table 1**

The average elemental content for PT0, PT25 and PT50 based on the EDS area maps in Fig. 3.

Sample	Ti (wt%)	Al (wt%)	V (wt%)
PT0	Bal.	6.3	3.9
PT25	Bal.	4.9	3.0
PT50	Bal.	3.0	1.8

content in PT25 (4.9 wt% and 3.0 wt%) and PT50 (3.0 wt% and 1.8 wt%) are close to the nominal and targeted compositions of the Ti-4.5Al-3V and Ti-3Al-2V alloys.

### 3.2. Microstructural evolution

Phase results measured by XRD of the as-built PT0, PT25, and PT50 are shown in Fig. 4. All the peaks of the as-built samples are assigned to titanium hexagonal close-packed (HCP) structure without obvious peaks of other titanium based phases such as the

**Table 2**

XRD data of as-built PT0, PT25, and PT50.

Sample	2 theta in (002)	2 theta in (101)	c/a
PT0	38.62	40.57	1.5966
PT25	38.59	40.51	1.5934
PT50	38.49	40.35	1.5918
Standard $\alpha$ -Ti HCP [32]	38.45	40.18	1.587

body-centered cubic (BCC) structure [15]. It is noteworthy that slight differences in peak position can be observed in the HCP structure for the different samples, as shown in Fig. 4(b) and Table 2. There is a left shift trend with the increase of addition of CP Ti. Based on the Bragg equation, the interplanar d-spacing value increases when the 2-theta degree position decreases (left shift). It is known that the atomic radius of vanadium (0.132 nm) and aluminum (0.143 nm) are smaller than titanium (0.147 nm) [30]. Therefore, the increase of Ti content and decrease of Al and V content (i.e. decreased solid

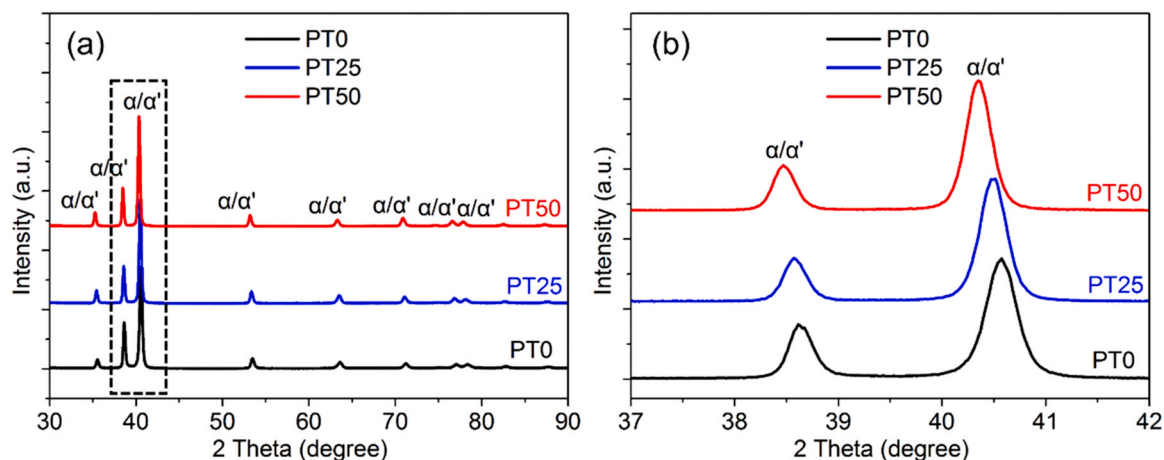


**Fig. 4.** XRD results of as-built PT0, PT25, and PT50.

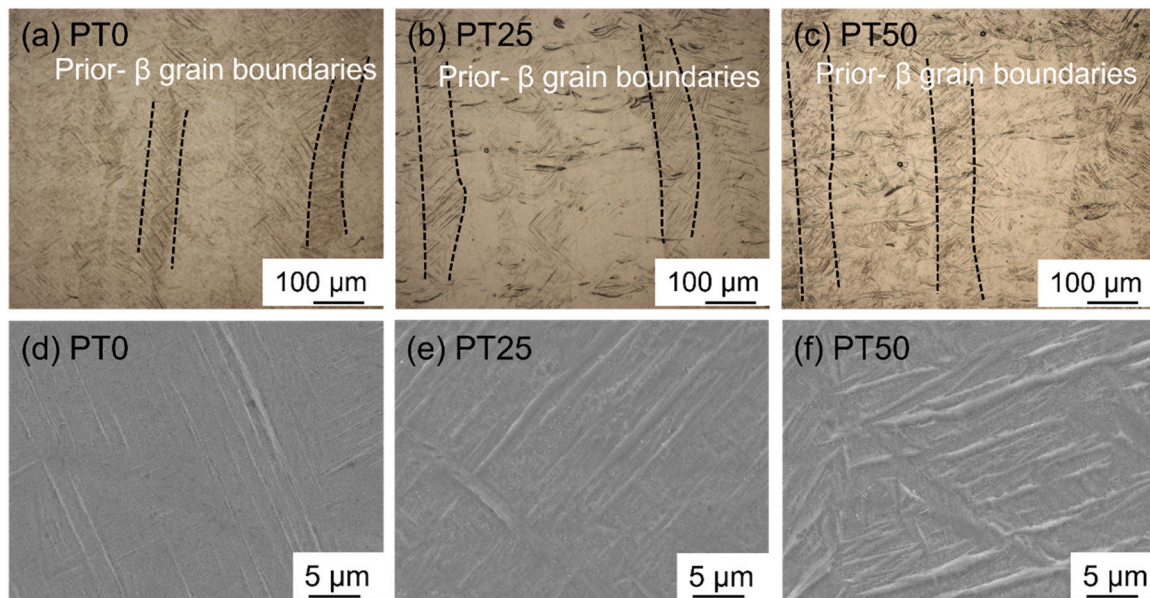


Fig. 5. Microstructure of as-built (a, d) PT0, (b, e) PT25, and (c, f) PT50 by OM and SEM.

solution effect) in PT25 and PT50 cause the increase in  $d$  value. The HCP  $c/a$  ratio can be evaluated by rearranging the Bragg equation [31]:

$$\sin\theta = \frac{\lambda}{2} \sqrt{\frac{4(h^2 + hk + k^2)}{3a^2} + \frac{l^2}{c^2}} \quad (1)$$

where  $\theta$  is the diffraction angle ( $2\theta$  related to peak position);  $\lambda$  is the wavelength of the X-ray (1.5406 Å);  $h$ ,  $k$  and  $l$  are Miller indices;  $a$  and  $c$  are the hexagonal lattice parameters. Six main diffraction peaks (crystal planes) are employed for calculations of  $c$ ,  $a$ , and  $c/a$ . The XRD results suggest that the  $c/a$  ratio is changed with a decreasing trend from 1.5966 for PT0 to 1.5918 for PT50 when CP Ti addition increases (see Table 2).

The etched microstructure of as-built PT0, PT25 and PT50 samples is shown in Fig. 5(a-c). All samples show typical prior- $\beta$  grain boundaries with fine martensite  $\alpha'$  that is mostly distributed at an angle of around  $\pm 45^\circ$  to the prior- $\beta$  grain boundaries [33]. The length of prior- $\beta$  grains was up to several mm and the thickness was around 60–80  $\mu\text{m}$ . These dimensions are close to the hatch distance (65  $\mu\text{m}$ ) used in this study and consistent with literature [34]. SEM images with high magnification in Fig. 5(d-f) show details of the martensite  $\alpha'$  structure. For PT0 (i.e. Ti-6Al-4V) with no CP Ti addition, a range of size-types of acicular martensite  $\alpha'$  structures (Fig. 5(d)) are observed. Nevertheless, the martensite  $\alpha'$  tends to form a lath structure with a larger thickness. The average martensite  $\alpha'$  thickness for as-built PT0, PT25 and PT50 are  $0.44 \pm 0.18 \mu\text{m}$ ,  $0.61 \pm 0.29 \mu\text{m}$ ,  $0.75 \pm 0.28 \mu\text{m}$ , respectively, which further indicates the effect of solid solution element Al and V on the martensite  $\alpha'$  structure [10].

Fig. 6 shows inverse pole figure maps and misorientation distribution of as-built PT0, PT25, and PT50. As-built PT50 shows evidence of wider martensite  $\alpha'$  structures compared to those of as-built PT0 (see Fig. 6(a-c)), which is consistent with SEM results. The misorientation distribution data for all samples are shown in Fig. 6(d-f). misorientation angle at  $\sim 63.26^\circ$  is the most common for all samples, which agrees well with other LPBF and DED Ti-6Al-4V parts with a columnar prior- $\beta$  structure [35,36]. The low angle grain boundary (LAGB, 2–10°, red color) and high angle grain boundary (HAGB, > 10°, blue color) of as-built PT0, PT25, and PT50 are shown in Fig. 7. A trend of increasing LAGBs (from 5.65% to 9.64–11.4%) with increasing CP Ti addition (see Fig. 7(a-c)) is observed. Kernel average

misorientation (KAM) maps associated with geometrically necessary dislocations (GND, accumulated in strain gradient fields caused by geometrical constraints of the crystal lattice.) for Ti-6Al-4V and developed Ti alloys are also compared, as shown in Fig. 7(d-f). The KAM value also increases with CP Ti addition in a similar trend to LAGB, which suggests there are increased local misorientation for PT25 (average  $\sim 0.820^\circ$ ) and PT50 (average  $\sim 0.869^\circ$ ) compared to PT0 (average  $\sim 0.656^\circ$ ).

### 3.3. Mechanical properties

Fig. 8 shows microhardness data for the as-built PT0, PT25, and PT50. There is an obvious decrease in hardness value with the addition of CP Ti, indicative of reduced strength. The hardness difference between PT0 (389.1 HV0.5) and PT25 (352.6 HV0.5), as well as between PT25 and PT50 (312.7 HV0.5) is around 38 HV0.5.

Fig. 9(a) shows tensile properties of as-built PT0, PT25, and PT50. The Young's modulus, tensile strength, yield strength, elongation at break are shown in Table 3. The Young's modulus in all samples is consistent, suggesting that the negligible effect of CP Ti addition into Ti-6Al-4V and the bonds within the martensite structure are all similar for the PT0, PT25 and PT50. It is clear that the mechanical properties of PT0 (Ti-6Al-4V) agree well with other LPBF produced Ti-6Al-4V [13,15,19], with a high strength (tensile strength over 1200 MPa) but poor ductility (less than 10%). The low ductility (elongation of 6.1% and 4.3%) of as-built PT0 by LPBF observed in this work is consistent with some literature [12–15,19] with elongation around 6% or below 6% in as-built Ti-6Al-4V by LPBF. Although there is a decreasing trend in tensile and yield strength with increasing CP Ti, the tensile and yield strength in PT50 are still relatively high (tensile strength  $\sim 1000$  MPa, yield strength  $\sim 900$  MPa). This is likely explained by the presence of the martensite  $\alpha'$  structure. Notably these properties may be also higher than that of as-cast Ti-6Al-4V alloy [37]. Importantly, the elongation (ductility) of PT50 significantly improved by over twice compared to the as-built state (from  $\sim 6.1\%$  and  $\sim 4.3\%$  for PT0 to  $\sim 13.1\%$  and  $\sim 12.3\%$  for PT50). The mechanical properties of the as-built PT50 also meet the annealed wrought Ti-6Al-4V standard [38]. Therefore, good strength and high ductility of as-built PT50 can be achieved through Ti-6Al-4V in-situ composition modification. Fig. 9(b) compares the properties in the present work with those of as-built and heat treated Ti-6Al-4V from

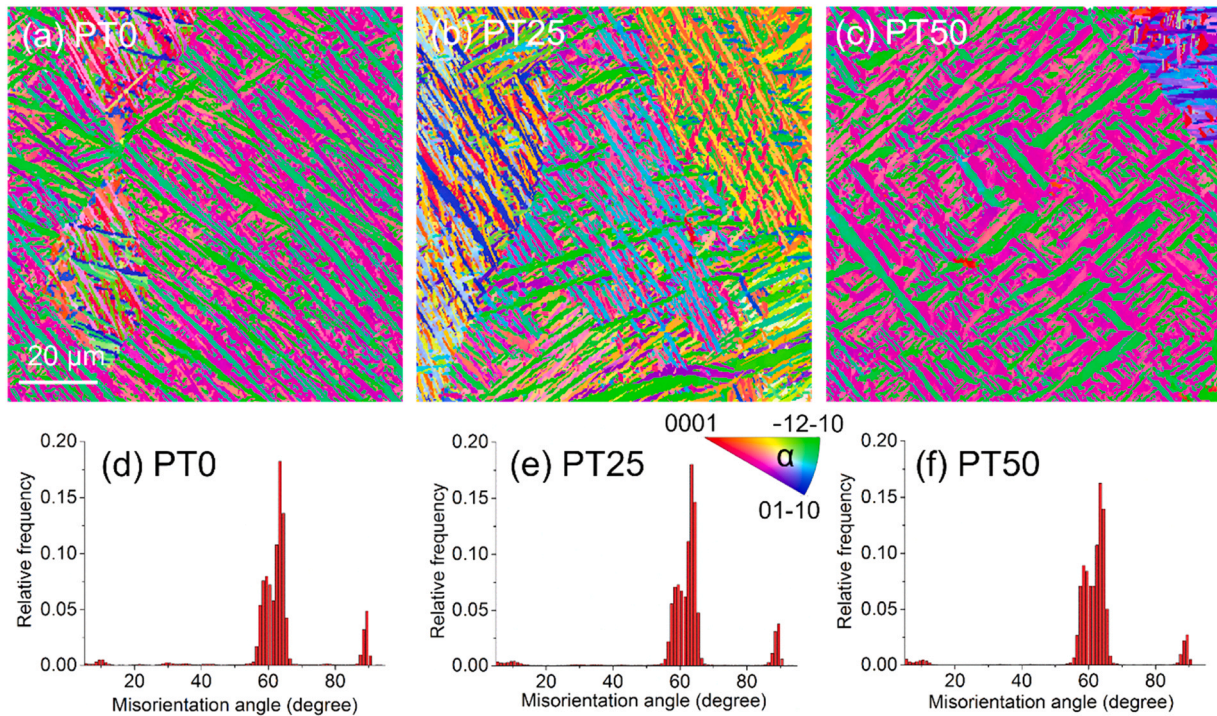


Fig. 6. Inverse pole figure maps (IPF, Z0 direction) and misorientation distribution of as-built (a, d) PT0, (b, e) PT25, and (c, f) PT50.

the literature. The mechanical properties of as-built PT50 are comparable with that of heat treated Ti-6Al-4V reported in literature.

The fracture surface of as-built PT0, PT25, and PT50 tensile bars are also presented and compared, shown in Fig. 10. For as-built PT0 (Ti-6Al-4V) with no CP Ti addition, typical terrace structure with some small areas of shallow dimples can be observed (see Fig. 10(a,

d)), which is consistent with literature [11]. The dominant fracture mode may be intergranular  $\alpha/\alpha'$  and along the prior- $\beta$  grain boundaries. The presence of terrace structure with limited dimples is indicative of the dominance of a brittle fracture mode of failure in LPBF as-built Ti-6Al-4V. With 25 wt% CP Ti addition, the dominance of terrace structure is reduced, and larger and deeper dimples

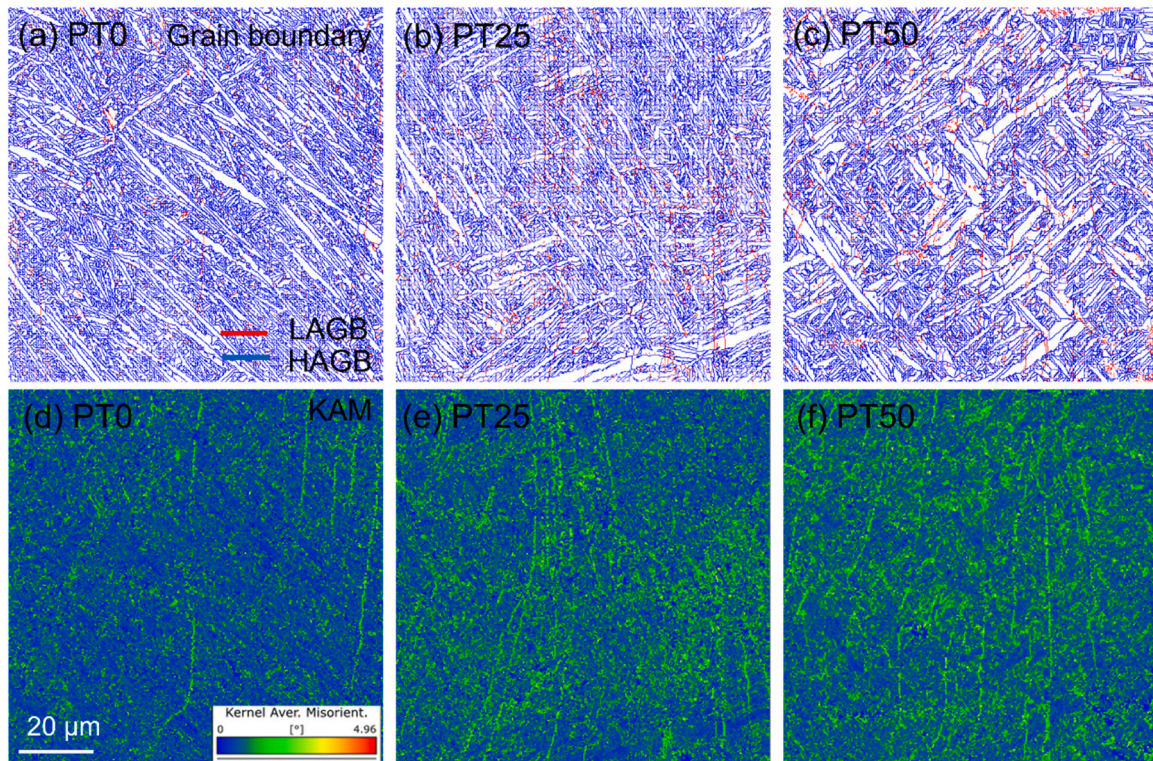
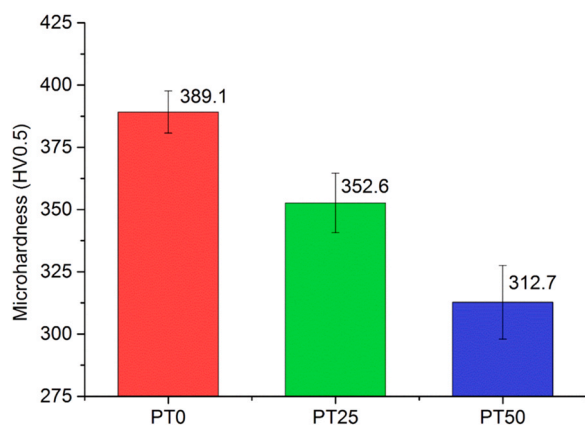


Fig. 7. Grain boundary distribution (low angle grain boundary LAGB, high angle grain boundary HAGB) and Kernel average misorientation (KAM) maps of as-built (a, d) PT0, (b, e) PT25, and (c, f) PT50.



**Fig. 8.** Microhardness results of the as-built PT0, PT25, and PT50 materials showing a reduction in hardness as CP Ti addition increases.

compared to as-built PT0, are common, as shown in Fig. 10(b, e). These characteristics imply a mixed brittle-ductile fracture mode in the case of PT25. PT50 (Fig. 10(c, f)) shows a fracture surface dominated by deeper and large dimples with no obvious terrace structure. This indicates the dominance of a ductile fracture mode and agrees well with the good ductility of as-built PT50 in tensile testing (see Fig. 9 and Table 3) and other heat treatment works [17,20].

## 4. Discussion

### 4.1. Chemical homogeneity

Although in-situ alloying has several merits including low cost and high speed for developing new alloys for LPBF, chemical homogeneity is a key and an inevitable challenge [44]. In contrast to other work in this field, here we perform in-situ alloying using a combination of pre-alloyed and corresponding elemental metal, i.e. Ti-6Al-4V with CP Ti. The nature of non-uniform elemental distribution observed in our work for LPBF PT25 and PT50 is distinct from that seen in other in-situ alloying work. LPBF parts printed from Ti-6Al-4V and CP Ti powder feedstocks showed less fluctuation in elemental concentration from the minor alloying elements across the part, in comparison to the in-situ alloying of Ti-6Al-4V using Ti, Al, and V element, seen by Simonelli et al. [45] for example. This is because at the length scale of tens to hundreds of  $\mu\text{m}$  both CP Ti and Ti-6Al-4V powder feedstocks present consistently above 90 wt% Ti with no area rich in Al and V. For Ti-6Al-4V fabricated by in-situ alloying with Ti, Al, and V elements, locally rich areas of Al or V may

**Table 3**

Young's modulus, tensile strength, yield strength, elongation at break of as-built PT0, PT25 and PT50.

Sample	Young's modulus E (GPa)	Tensile strength (MPa)	Yield strength (MPa)	Elongation (%)
PT0-1	115	1285	1128	6.1
PT0-2	116	1271	1118	4.3
PT25-1	119	1155	1009	8.7
PT25-2	112	1132	1011	8.5
PT50-1	118	1012	895	13.1
PT50-2	115	993	890	12.3

form with high concentration (over 10%) at these length scales. The precise contribution of these as a function of number density and size is difficult to appraise. It is clear that laser melting and cooling process during the LPBF is limited in achieving the necessary melt lifetime or melt size to yield sufficient homogenization of separate elements in typical powder size ranges. From microhardness results (see Fig. 8), although there are fluctuations in different areas even for pre-alloyed Ti-6Al-4V due to the presence of  $\alpha$  and martensite  $\alpha'$ , these fluctuations are not significant in comparison to the absolute value ranges of almost microhardness values, whereby minimum overlap of hardness ranges is seen (367.8–407.7 HV0.5 for PT0, 327.6–374.8 HV0.5 for PT25, 277.9–341.6 HV0.5 for PT50). This also suggests good metallurgical fusion of Al and V for PT25 and PT50.

Although segregation can be observed for Al and V, this segregation may not be serious (non-uniform area is around 1.4% for PT25 and around 3.4% for PT50 measured by high magnification (1000X) BSE images while around 0.48% for PT25 and around 0.99% for PT50 measured by low magnification (150X) BSE images). This suggests that although local segregation is formed, the whole segregation may be limited. This helps to assume the compositions to be closely representative of pre-alloyed equivalents, which indicates what is achievable of composition tailoring (composition design) to obtain desired mechanical properties. This kind of low level segregation may have a limited or minor effect on mechanical properties as expected and good mechanical properties achieved in this work. In-situ tensile testing experiments may be helpful to investigate the role of segregation on mechanical properties. Although difference of particle size used for CP Ti and Ti-6Al-4V, the segregation during spreading in the powder bed may also not be significant based on relative density and elemental segregation results. Further work should be considered to clarify the effect of particle size on powder segregation during spreading in the powder bed. There are some possible ways to achieve excellent homogeneity and eliminate segregation. Firstly, a different energy input and creation of deeper melt

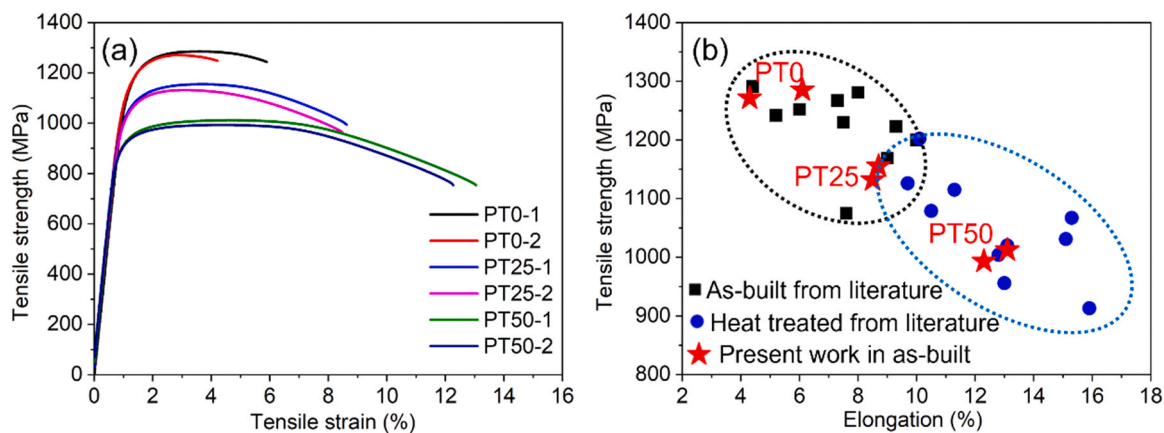


**Fig. 9.** Tensile properties (a) of as-built PT0, PT25, PT50 and (b) comparison with as-built and heat-treated Ti-6Al-4V by LPBF from literature [11,13–21,23,32,39–43] showing comparable mechanical properties in PT50 with heat-treated Ti-6Al-4V.

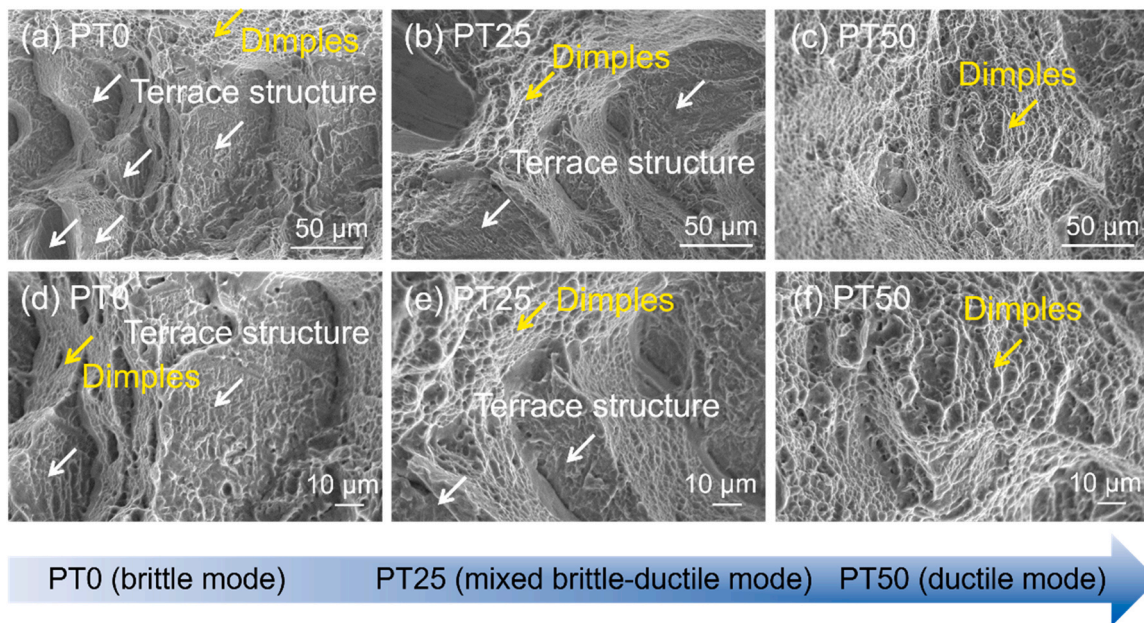


**Fig. 10.** Fracture surface morphology of as-built (a, d) PT0, (b, e) PT25, and (c, f) PT50 showing the fracture mode transferred from brittle to mixed brittle-ductile to ductile mode.

pools could enhance mixing [46]. Segregation could also be reduced significantly by remelting each processing layer as demonstrated by Brodie et al. [47]. Heat treatment is also a practical way to reduce segregation. It is thought that a suitable heat treatment should be conducted in the high region of the  $\alpha + \beta$  phase field (below the  $\beta$  transus temperature) to enhance solid state diffusion of the elements. It would be interesting to further optimize processing parameters to achieve a more uniform composition and better strength-ductility in the as-built state.

#### 4.2. Composition-dependent microstructure

Fig. 11 shows a summary of the relationship between composition and microstructure for the PT0, PT25 and PT50 in this work. It is

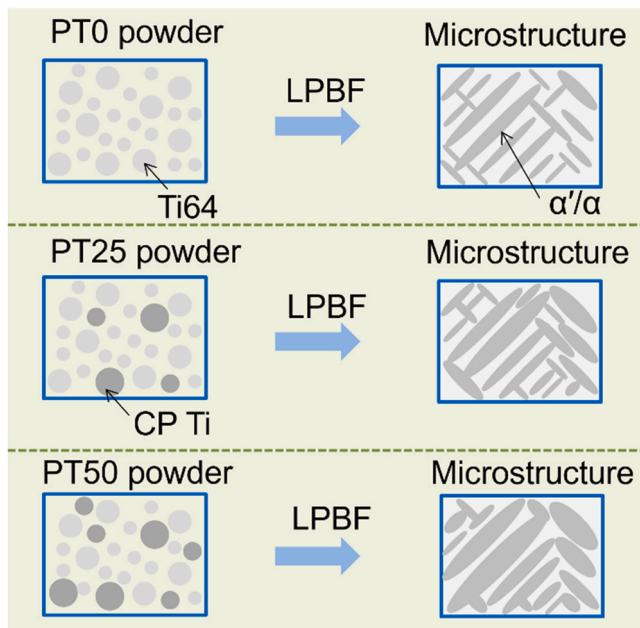


**Fig. 11.** The summary of composition-microstructure relationship showing the response to formulation change in the simply mixed feedstock.

known that there are usually two martensitic types ( $\alpha'$  and  $\alpha''$ ) after rapid cooling for Ti alloys [10]. It is believed that  $\alpha'$  is the main phase for all Ti alloys in this work rather than the  $\alpha''$  phase. Firstly,  $\alpha$  and  $\alpha'$  Ti have an hexagonal close-packed (HCP) structure while  $\alpha''$  Ti is an orthorhombic structure [10,31]. Using XRD it may be difficult to distinguish between  $\alpha$  and  $\alpha'$  while it is possible to detect  $\alpha''$  from  $\alpha$  and  $\alpha'$ , which is confirmed by an  $\alpha + \beta$  type titanium (Ti-6Al-2Sn-4Zr-6Mo) by LPBF by Carrozza et al. [31]. Secondly,  $\alpha''$  tends to be observed in alloys with higher concentration of  $\beta$  stabilizers. Considering that additions of CP Ti decrease the starting equivalent Mo content ( $Mo_{eq}$ ) of Ti-6Al-4V, it is thought that the formation of martensite  $\alpha''$  in developed alloys is unlikely [10]. It is also noteworthy that structures dominated by  $\alpha''$  martensite usually shows low yield strength (around 500–600 MPa) [31,48]. In this work, the yield strengths of the PT0, PT25, PT50 are around 1122 MPa, 1010 MPa, 893 MPa respectively. Finally, some literature [49,50] presenting martensite  $\alpha'$  of Ti-3Al-2.5V (close to PT50) after rapid cooling (like during welding [50]) can be found. The PT25 and PT50 LPBF built Ti alloys present wider martensite  $\alpha'$  structures compared to PT0. The reduced Al and V solute content in the developed alloys results in this increased width of the martensite  $\alpha'$  structure (see Figs. 5 and 6). This phenomenon is well understood [10]. High solute content Ti alloys (Ti-6Al-4V) usually show acicular martensite resulting from a lower martensitic transformation temperature, while for more dilute solute content alloys (e.g. PT25 and PT50), lath (also named massive or packet) martensite might be typically observed caused by a higher martensite transformation temperature.

#### 4.3. Composition-dependent mechanical properties

##### 4.3.1. Mechanisms of ductile behavior

The  $c/a$  lattice ratio is a crucial factor in determining the deformation mode of  $\alpha$  and  $\alpha + \beta$  titanium alloys. High  $c/a$  ratio (over 1.630) Ti alloys tend to show basal slip and twinning while low  $c/a$  ratio Ti alloys (less than 1.630) may activate basal slip, prismatic slip, and pyramidal slip [51]. It is known that CP Ti with low  $c/a$  ratio ( $\sim 1.587$ ) by LPBF usually presents good ductility [4,27,32]. As mentioned before, the  $c/a$  ratios in PT0, PT25, and PT50 are 1.5966, 1.5934 and 1.5918, respectively. Basal slip  $\{0002\} <11\bar{2}0>$  dominates in Ti-6Al-4V (PT0) made by LPBF manifesting in poor ductility in the as-

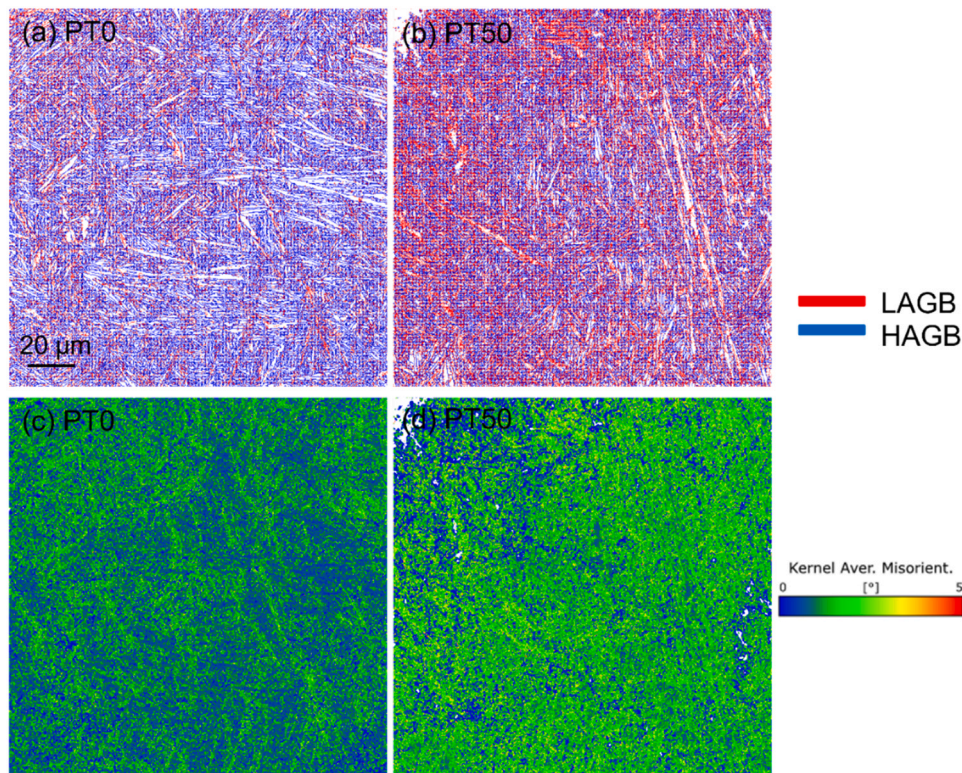


Fig. 12. The comparison of grain boundary distribution (a) and (b), and KAM (c) and (d) in as-built PT0 and PT50 after tensile testing.

built state [18] as higher  $c/a$  ratios with high Al content increase the basal plane spacing while reducing the prismatic plane spacing [24]. The increased prismatic plane spacing when  $c/a$  ratio decreases therefore facilitates the prismatic slip rather than basal slip [52]. The decreased  $c/a$  ratio in PT25 and PT50 may show a lower  $CRSS_{prism}/CRSS_{basal}$  (critical resolved shear stress, CRSS) ratio than that of PT0. As a result, multiple slips may be activated during deformation, which is confirmed by comparison of Ti-6Al-4V ( $c/a$  ratio 1.596) and Ti-4Al-4V ( $c/a$  ratio 1.594) [24]. In addition, tensile fractured samples analysed by EBSD (Fig. 12) in this work also indicate enhanced dislocation slip when CP Ti addition increases. EBSD KAM maps associated with geometrically necessary dislocations for PT50 after tensile testing show more regions with higher local misorientation (average  $\sim 1.448^\circ$ ) than that of PT0 (average  $\sim 1.022^\circ$ ), with a high density of dislocations indicative of enhanced dislocation slip. Good ductility caused by a dominance of dislocation slip was also demonstrated in EBSD KAM by Qiu et al. [53] in an LPBF printed beta titanium alloy. Meanwhile, Fig. 12 shows that the number of LAGBs in PT50 after tensile testing is also significantly higher (44.9%) compared to PT0 after tensile testing (24.2%). The LAGB is normally composed of a periodic crystal dislocation arrangement [51]. Hence, extensive dislocation slip events may be expected in PT50 giving rise to higher ductility. In this work, PT0, PT25 and PT50 mainly show the  $\alpha/\alpha'$  Ti-HCP phase in the as-built condition as confirmed by microscopy and XRD, which suggests the negligible effect of retained  $\beta$  phase on ductility.

Therefore, it is thought that the decreased  $c/a$  ratio makes an important contribution to the enhanced ductility of as-built Ti-Al-V based alloys. The increased number of LAGBs in as-built PT50 may also contribute to increased ductility. Chen et al. explained this by suggesting [54] that LAGBs may help to give a more stable/uniform deformation and a higher failure tolerance, thereby providing a more balanced strength and ductility at multiple scales.

#### 4.3.2. Strength mechanisms

In this work, the yield strength and tensile strength of PT25 and PT50 decreased compared to PT0 (see Fig. 9 and Table 3). The strengthening mechanisms operating in PT0, PT25 and PT50 can be compared at least semi-quantitatively. The yield strength ( $\sigma_{YS}$ ) of Ti alloys can be evaluated by the following equation [24]:

$$\sigma_{YS} = \sigma_0 + \sigma_{SS} + \sigma_{GB} + \sigma_{Dis} \quad (2)$$

To facilitate comparison, one can assume  $\sigma_0$  as the yield strength of Pure Ti. The term  $\sigma_{SS}$ , the solid solution strengthening,  $\sigma_{GB}$ , grain boundary strengthening and  $\sigma_{Dis}$  dislocation strengthening deserve some considerations. Assuming ideal mixing, the strengthening effect of solute elements in solid solutions can be described by [37]:

$$\sigma_{SS} = B_i X_i^{2/3} \quad (3)$$

where  $B_i$  is the strengthening coefficient for the solute  $i$  and  $X_i$  is the atomic concentration of the solute  $i$ . The cumulative strengthening effect of solute elements in developed Ti alloy can therefore be expressed by [55]:

$$\sigma_{SS} = \left( \sum_i B_i^{2/3} X_i \right)^{2/3} \quad (4)$$

One can be expected that PT25 and PT50 with less Al and V content may show lower solid solution strengthening (lower  $X_i$  in Al and V content) than that of PT0.

The grain boundary strengthening  $\sigma_{GB}$  is often expressed via the Hall-Petch equation:

$$\sigma_{GB} = \frac{k}{\sqrt{d}} \quad (5)$$

where  $k$  is the Hall-Petch coefficient, and  $d$  is the martensite  $\alpha'$  thickness [43]. Assuming a constant of  $k$  equal to  $300 \text{ MPa } \mu\text{m}^{-1/2}$  [56], and the value of martensite  $\alpha'$  thickness reported in Section 3.2,

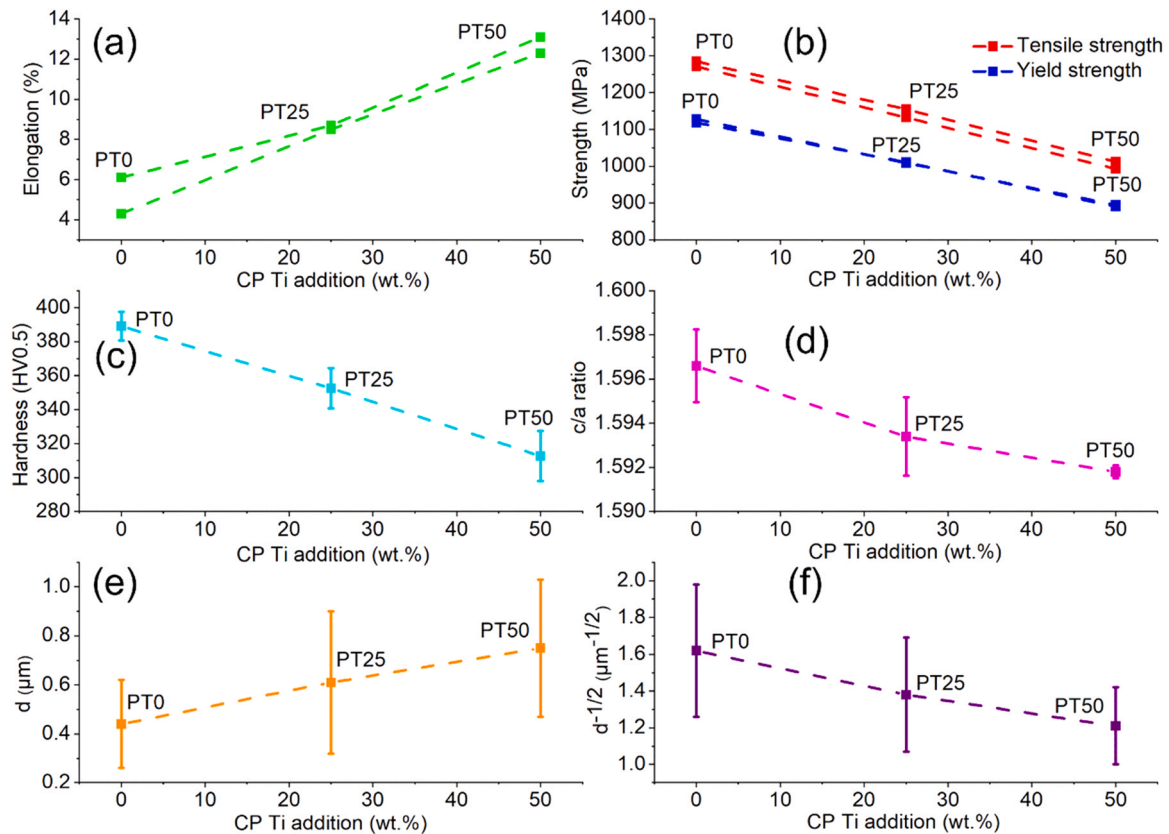


**Fig. 13.** The relationships between (a) ductility, (b) tensile and yield strength, (c) microhardness, (d) *c/a* ratio, (e) martensite  $\alpha'$  thickness, (f) the inverse square root of martensite  $\alpha'$  thickness and CP Ti addition.

a decreased trend of grain boundary strengthening can be estimated when CP Ti addition are carried out.

The dislocation strengthening ( $\sigma_{Dis}$ ) contribution can be described by the Bailey-Hirsch formula as follows [57,58]:

$$\sigma_{Dis} = M\alpha_p Gb\sqrt{\rho} \quad (6)$$

$$\rho = \frac{12Es}{(1+2\nu^2)Gb} \frac{\varepsilon_{trans}^2}{d^2} \quad (7)$$

where  $M$  is the Taylor factor,  $\alpha_p$  is a constant coefficient,  $G$  is the shear modulus of  $\alpha'$ ,  $b$  is the Burgers vector length, and  $\rho$  is the dislocation density.  $E$  is the Young's modulus,  $s$  is the lath boundary thickness,  $\nu$  is the Poisson's ratio, and  $\varepsilon_{trans}$  is the transformation strain from  $\beta$  to  $\alpha'$ ,  $d$  is martensite  $\alpha'$  thickness. The  $\sigma_{Dis}$  is therefore mainly related to the  $d$  value for different composition in Ti alloys [24]. Therefore,  $\sigma_{Dis}$  may be also expected to decrease for PT50 and PT25, respectively.

Relationships for strength, ductility, hardness, *c/a* ratio, martensite  $\alpha'$  thickness, and inverse square root of martensite  $\alpha'$  thickness for CP Ti addition with 0 wt%, 25 wt%, and 50 wt% are shown in Fig. 13. For all variables, clear trends are seen which link composition, microstructure and mechanical properties. Therefore, tunable, predictable, and desirable mechanical properties may be possible through the controlled addition of CP Ti into Ti-6Al-4V by LPBF.

#### 4.4. Materials adaption for Ti alloys by LPBF

In this work, Ti-Al-V based alloys with nominal Ti-4.5Al-3V (close to ~TA17, Ti-4Al-2V) and Ti-3Al-2V (close to ~Grade 9, Ti-3Al-2.5V) via the addition of CP Ti were successfully fabricated by LPBF. It is clear that the tensile strength of ~1003 MPa of nominal Ti-3Al-2V is significantly higher than that of Ti-3Al-2.5V by conventional

manufacturing (~600–850 MPa) [59–61]. This increased strength of Ti-3Al-2V by LPBF could be ascribed to the fine martensite structure, which makes it possible to achieve comparable mechanical properties of Ti-6Al-4V by casting [37]. In-situ alloying with desired Ti-6(1-x)Al-4(1-x)V ( $x$  is the CP Ti content) through blending with different CP Ti content into Ti-6Al-4V by LPBF can be achieved. This approach demonstrates the controllability of the martensite structure and therefore mechanical properties.

This study improves the poor ductility of as-built Ti-6Al-4V in a simple and accessible way, which is potentially more practical and economical compared to in-situ heat treatment and post-heat treatment. The addition of CP Ti inside Ti-6Al-4V, thereby reducing the Al and V content, also has the potential to increase the range of applications for this material type, including for biocompatibility purposes given the reduction of Al and V, while having better strength than CP Ti.

In summary, material adaption for Ti-6Al-4V through in-situ alloying with CP Ti addition is viable for the tuning of microstructure and mechanical properties to meet desired requirements in the as-built state. In addition, CP Ti can be also a good composition modifier for other Ti alloys to obtain good as-built properties. For example, as-built near  $\alpha$  Ti alloy Ti-6.5Al-2Zr-1Mo-1V (TA15) by LPBF also shows high strength and poor ductility [62,63], and this in-situ composition modification method may be also feasible for improving the balance of strength-ductility of as-built parts. More importantly, among Ti alloys by LPBF, non-equilibrium structures may be formed based on the  $\beta$  stabilized element content (i.e.  $M_{0eq}$ ) via fast cooling rates, varying from martensite  $\alpha'$ , martensite  $\alpha''$  to metastable  $\beta$  (may include  $\omega$  phase) and stable  $\beta$ . The non-equilibrium structure of as-built Ti alloys by LPBF may be also tailored with proper CP Ti addition [10]. For example, high solute content Ti alloys (like Ti-6Al-2Sn-4Zr-6Mo) with martensite  $\alpha''$  and low yield strength produced by

LPBF [31] may be changed to a martensite  $\alpha'$  structure via in-situ CP Ti addition. Also, commercial metastable or stable  $\beta$  Ti alloys with proper in-situ CP Ti addition by LPBF may activate the transformation-induced plasticity (TRIP) and/or twinning-induced plasticity (TWIP) effect to achieve improved strength and ductility. Therefore, the in-situ CP Ti addition in Ti alloys is a useful way to tune the microstructure and mechanical properties for the wider LPBF community. Other alloy systems should also investigate the use of this approach (e.g. pure Fe with steels, pure Ni with Ni superalloys), and future work of the authors will interrogate such systems.

## 5. Conclusions

In this work, a simple in-situ composition modification strategy is employed for Ti-6Al-4V alloy by LPBF to address the common issue of poor ductility while maintaining good strength (~1000 MPa) due to the presence of a martensitic  $\alpha'$  structure. The main results can be concluded as follows:

1. Developed Ti alloys with nominal Ti-4.5Al-3 V (PT25) and Ti-3Al-2 V (PT50) can be obtained by using in-situ composition modification of Ti-6Al-4 V (PT0) alloy via CP Ti addition. Good relative density of PT25 and PT50 can be achieved using the same processing parameters as PT0.
2. Some non-uniform areas are observed in PT25 and PT50. The martensite  $\alpha'$  thickness increases when CP Ti addition increases. There is a trend for acicular to lath transformation for martensite  $\alpha'$  structure with increasing addition of CP Ti.
3. The strength and microhardness decrease while ductility increases when CP Ti addition increases. High strength-ductility for as-built PT50 can be achieved with UTS~1000 MPa, YS~900 MPa, and EL~13%, which meets the wrought Ti-6Al-4V standard. The mechanical properties can therefore be facily manipulated by proper CP Ti addition.
4. The decreased c/a ratio to increase dislocation slip is thought to contribute to the enhanced ductility for PT25 and PT50. The LAGB and KAM results by EBSD from the tensile fractured sample confirm the dislocation slip enhancement resulting in good ductility of the modified Ti alloy. The increased number of LAGBs for PT50 may also facilitate this improved ductility. The reduced strength is mainly explained by decreased solid solution strengthening and grain boundary strengthening.

This composition tailoring (composition design) method similar to pre-alloying via easy mixing with Ti-6Al-4 V and CP Ti can achieve a good balance of strength and ductility of Ti alloys. This work may industrial interested for building Ti alloy parts with balanced strength-ductility in a rapid, simple and economical manner. This in-situ composition tailoring strategy may be possible to apply in other Ti alloys, steels, and Ni-based superalloys to achieve a more balanced and tailored strength-ductility or other desired properties, which may be an economical and practical strategy for materials adaption and development in LPBF.

## CRedit authorship contribution statement

**Xi Du:** Conceptualization, Methodology, Investigation, Formal analysis, Writing – original draft. **Marco Simonelli:** Conceptualization, Resources, Formal analysis, Writing – review & editing, Supervision. **James W. Murray:** Conceptualization, Formal analysis, Writing – review & editing, Supervision. **Adam T. Clare:** Conceptualization, Formal analysis, Writing – review & editing, Supervision, Funding acquisition.

## Data availability

Data will be made available on request.

## Declaration of Competing Interest

The authors declare that they have no known competing financial interests or personal relationships that could have appeared to influence the work reported in this paper.

## Acknowledgments

Xi Du thanks China Scholarship Council (No. 201908310091) for Ph.D. sponsorship. The authors would like to thank Mr. Mark East and Mr. Mark Hardy for their assistance in the laboratory work at the Centre for Additive Manufacturing. Xi Du also thanks Dr Nigel Neate from nano- and micro-research centre (nmRC) in the University of Nottingham for training and access of SEM (EDS) and EBSD. Adam Clare is grateful for the support by the Royal Academy of Engineering, [RCSRF1920/9/27].

## References

- [1] T. DebRoy, H.L. Wei, J.S. Zuback, T. Mukherjee, J.W. Elmer, J.O. Milewski, A.M. Beese, A. Wilson-Heid, A. De, W. Zhang, Additive manufacturing of metallic components—process, structure and properties, *Prog. Mater. Sci.* 92 (2018) 112–224, <https://doi.org/10.1016/j.pmatsci.2017.10.001>
- [2] C. Tan, F. Weng, S. Sui, Y. Chew, G. Bi, Progress and perspectives in laser additive manufacturing of key aeroengine materials, *Int. J. Mach. Tools Manuf.* 170 (2021) 103804, <https://doi.org/10.1016/j.ijmactools.2021.103804>
- [3] A.T. Clare, R.S. Mishra, M. Merklein, H. Tan, I. Todd, L. Chechik, J. Li, M. Bambach, Alloy design and adaptation for additive manufacture, *J. Mater. Process. Technol.* 299 (2022), <https://doi.org/10.1016/j.jmatprotec.2021.117358>
- [4] J. Zhang, Y. Liu, M. Bayat, Q. Tan, Y. Yin, Z. Fan, S. Liu, J. Henri, M. Dargusch, M. Zhang, Achieving high ductility in a selectively laser melted commercial pure-titanium via in-situ grain refinement, *Scr. Mater.* 191 (2021) 155–160, <https://doi.org/10.1016/j.scriptamat.2020.09.023>
- [5] T. Zhang, C. Liu, Design of titanium alloys by additive manufacturing: a critical review, *Adv. Powder Mater.* 1 (2022) 100014, <https://doi.org/10.1016/j.apmate.2021.11.001>
- [6] N.T. Aboulkhair, M. Simonelli, L. Parry, I. Ashcroft, C. Tuck, R. Hague, Progress in materials science 3D printing of aluminium alloys: additive manufacturing of aluminium alloys using selective laser melting, *Prog. Mater. Sci.* 106 (2019) 100578, <https://doi.org/10.1016/j.pmatsci.2019.100578>
- [7] H.R. Kotadia, G. Gibbons, A. Das, P.D. Howes, A review of laser powder bed fusion additive manufacturing of aluminium alloys: microstructure and properties, *Addit. Manuf.* 46 (2021) 102155, <https://doi.org/10.1016/j.addma.2021.102155>
- [8] Y.T. Tang, C. Panwisawas, J.N. Ghossein, Y. Gong, J.W.G. Clark, A.A.N. Németh, D.G. McCartney, R.C. Reed, Alloys-by-design: application to new superalloys for additive manufacturing, *Acta Mater.* 202 (2021) 417–436, <https://doi.org/10.1016/j.actamat.2020.09.023>
- [9] Salomé Sanchez, P. Smith, Z. Xu, G. Gaspard, C.J. Hyde, W.W. Wits, I.A. Ashcroft, H. Chen, A.T. Clare, Powder bed fusion of nickel-based superalloys: a review, *Int. J. Mach. Tools Manuf.* 165 (2021), <https://doi.org/10.1016/j.ijmactools.2021.103729>
- [10] Gerd Lütjering, James C. Williams, *Titanium*, 2007.
- [11] M. Simonelli, Y.Y. Tse, C. Tuck, Effect of the build orientation on the mechanical properties and fracture modes of SLM Ti-6Al-4V, *Mater. Sci. Eng. A* 616 (2014) 1–11, <https://doi.org/10.1016/j.msea.2014.07.086>
- [12] Y. Yang, Y.J. Liu, J. Chen, H.L. Wang, Z.Q. Zhang, Y.J. Lu, S.Q. Wu, J.X. Lin, Crystallographic features of  $\alpha$  variants and  $\beta$  phase for Ti-6Al-4V alloy fabricated by selective laser melting, *Mater. Sci. Eng. A* 707 (2017) 548–558, <https://doi.org/10.1016/j.msea.2017.09.068>
- [13] S. Liu, Y.C. Shin, Additive manufacturing of Ti6Al4V alloy: a review, *Mater. Des.* 164 (2019) 107552, <https://doi.org/10.1016/j.matdes.2018.107552>
- [14] X. Chen, C. Qiu, In-situ development of a sandwich microstructure with enhanced ductility by laser reheating of a laser melted titanium alloy, *Sci. Rep.* 10 (2020) 1–12, <https://doi.org/10.1038/s41598-020-72627-x>
- [15] Z. Zou, M. Simonelli, J. Katrib, G. Dimitrakakis, R. Hague, Microstructure and tensile properties of additive manufactured Ti-6Al-4V with refined prior- $\beta$  grain structure obtained by rapid heat treatment, *Mater. Sci. Eng. A* 814 (2021) 141271, <https://doi.org/10.1016/j.msea.2021.141271>
- [16] B. Vrancken, L. Thijs, J.P. Kruth, J. Van Humbeeck, Heat treatment of Ti6Al4V produced by selective laser melting: microstructure and mechanical properties, *J. Alloy. Compd.* 541 (2012) 177–185, <https://doi.org/10.1016/j.jallcom.2012.07.022>
- [17] J. Ju, J. Li, C. Yang, K. Wang, M. Kang, J. Wang, Evolution of the microstructure and optimization of the tensile properties of the Ti – 6Al – 4V alloy by selective laser

- melting and heat treatment, *Mater. Sci. Eng. A* 802 (2021) 140673, <https://doi.org/10.1016/j.msea.2020.140673>
- [18] D. Zhang, L. Wang, H. Zhang, A. Maldar, G. Zhu, W. Chen, J.S. Park, J. Wang, X. Zeng, Effect of heat treatment on the tensile behavior of selective laser melted Ti-6Al-4V by in situ X-ray characterization, *Acta Mater.* 189 (2020) 93–104, <https://doi.org/10.1016/j.actamat.2020.03.003>
- [19] Z. Zou, M. Simonelli, J. Katrib, G. Dimitrakis, R. Hague, Refinement of the grain structure of additive manufactured titanium alloys via epitaxial recrystallization enabled by rapid heat treatment, *Scr. Mater.* 180 (2020) 66–70, <https://doi.org/10.1016/j.scriptamat.2020.01.027>
- [20] S.A. Etesami, B. Fotovvati, E. Asadi, Heat treatment of Ti-6Al-4V alloy manufactured by laser-based powder-bed fusion\_ process, microstructures, and mechanical properties correlations, *J. Alloy. Compd.* 895 (2022) 162618, <https://doi.org/10.1016/j.jallcom.2021.162618>
- [21] W. Xu, M. Brandt, S. Sun, J. Elambasseril, Q. Liu, K. Latham, K. Xia, M. Qian, Additive manufacturing of strong and ductile Ti-6Al-4V by selective laser melting via in situ martensite decomposition, *Acta Mater.* 85 (2015) 74–84, <https://doi.org/10.1016/j.actamat.2014.11.028>
- [22] W. Xu, E.W. Lui, A. Pateras, M. Qian, M. Brandt, In situ tailoring microstructure in additively manufactured Ti-6Al-4V for superior mechanical performance, *Acta Mater.* 125 (2017) 390–400, <https://doi.org/10.1016/j.actamat.2016.12.027>
- [23] J. Liu, Q. Sun, C. Zhou, X. Wang, H. Li, K. Guo, J. Sun, Achieving Ti6Al4V alloys with both high strength and ductility via selective laser melting, *Mater. Sci. Eng. A* 766 (2019), <https://doi.org/10.1016/j.msea.2019.138319>
- [24] L. Wang, Z. Song, X. Zhang, J. Almer, G. Zhu, Y. Chen, Developing ductile and isotropic Ti alloy with tailored composition for laser powder bed fusion, *Addit. Manuf.* (2022) 102656, <https://doi.org/10.1016/j.addma.2022.102656>
- [25] (<https://www.carpentertechnology.com/>).
- [26] (<https://www.advancedpowders.com/>).
- [27] H. Attar, M. Calin, L.C. Zhang, S. Scudino, J. Eckert, Manufacture by selective laser melting and mechanical behavior of commercially pure titanium, *Mater. Sci. Eng. A* 593 (2014) 170–177, <https://doi.org/10.1016/j.msea.2013.11.038>
- [28] L.H. Qian, S.C. Wang, Y.H. Zhao, K. Lu, Microstrain effect on thermal properties of nanocrystalline Cu, *Acta Mater.* 50 (2002) 3425–3434, [https://doi.org/10.1016/S1359-6454\(02\)00155-6](https://doi.org/10.1016/S1359-6454(02)00155-6)
- [29] P. Kumar, U. Ramamurthy, Microstructural optimization through heat treatment for enhancing the fracture toughness and fatigue crack growth resistance of selective laser melted Ti-6Al-4V alloy, *Acta Mater.* 169 (2019) 45–59, <https://doi.org/10.1016/j.actamat.2019.03.003>
- [30] J. Jiang, Z. Ren, Z. Ma, T. Zhang, P. Zhang, D.Z. Zhang, Z. Mao, Mechanical properties and microstructural evolution of TA15 Ti alloy processed by selective laser melting before and after annealing, *Mater. Sci. Eng. A* 772 (2020) 138742, <https://doi.org/10.1016/j.msea.2019.138742>
- [31] A. Carrozza, A. Aversa, P. Fino, M. Lombardi, A study on the microstructure and mechanical properties of the Ti-6Al-2Sn-4Zr-6Mo alloy produced via laser powder bed fusion, *J. Alloy. Compd.* 870 (2021) 159329, <https://doi.org/10.1016/j.jallcom.2021.159329>
- [32] D. Gu, Y. Hagedorn, W. Meiners, G. Meng, Densification behavior, microstructure evolution, and wear performance of selective laser melting processed commercially pure titanium, *Acta Mater.* 60 (2012) 3849–3860, <https://doi.org/10.1016/j.actamat.2012.04.006>
- [33] J. Yang, H. Yu, J. Yin, M. Gao, Z. Wang, X. Zeng, Formation and control of martensite in Ti-6Al-4V alloy produced by selective laser melting, *Mater. Des.* 108 (2016) 308–318, <https://doi.org/10.1016/j.matdes.2016.06.117>
- [34] P. Kumar, O. Prakash, U. Ramamurthy, Micro- and meso-structures and their influence on mechanical properties of selectively laser melted Ti-6Al-4V, *Acta Mater.* 154 (2018) 246–260, <https://doi.org/10.1016/j.actamat.2018.05.044>
- [35] H. Wang, Q. Chao, L. Yang, M. Cabral, Z.Z. Song, B.Y. Wang, S. Primig, W. Xu, Z.B. Chen, S.P. Ringer, X.Z. Liao, Q. Chao, L. Yang, M. Cabral, Z.Z. Song, B.Y. Wang, S. Primig, Introducing transformation twins in titanium alloys: an evolution of  $\alpha$ -variants during additive manufacturing, *Mater. Res. Lett.* 9 (3) (2021) 119–126, <https://doi.org/10.1080/21663831.2020.1850536>
- [36] S.L. Lu, C.J. Todaro, Y.Y. Sun, T. Song, M. Brandt, M. Qian, Variant selection in additively manufactured alpha-beta titanium alloys, *J. Mater. Sci. Technol.* 113 (2022) 14–21, <https://doi.org/10.1016/j.jmst.2021.10.021>
- [37] T. Zhang, J. Zhu, T. Yang, J. Luan, H. Kong, W. Liu, A new  $\alpha + \beta$  Ti-alloy with refined microstructures and enhanced mechanical properties in the as-cast state, *Scr. Mater.* 207 (2022) 114260, <https://doi.org/10.1016/j.scriptamat.2021.114260>
- [38] (<https://www.astm.org/f1472-14.html>).
- [39] (<https://www.slm-solutions.com>).
- [40] L. Liu, C. Chen, R. Zhao, X. Wang, H. Tao, S. Shuai, J. Wang, H. Liao, Z. Ren, In-situ nitrogen strengthening of selective laser melted Ti6Al4V with superior mechanical performance, *Addit. Manuf.* 46 (2021) 102142, <https://doi.org/10.1016/j.addma.2021.102142>
- [41] A. Gullane, J.W. Murray, C.J. Hyde, S. Sankare, A. Evirgen, A.T. Clare, On the use of multiple layer thicknesses within laser powder bed fusion and the effect on mechanical properties, *Mater. Des.* 212 (2021) 110256, <https://doi.org/10.1016/j.matdes.2021.110256>
- [42] Y. Xu, D. Zhang, Y. Guo, S. Hu, X. Wu, Y. Jiang, Microstructural tailoring of as-selective laser melted Ti6Al4V alloy for high mechanical properties, *J. Alloy. Compd.* 816 (2020) 152536, <https://doi.org/10.1016/j.jallcom.2019.152536>
- [43] S. Cao, Y. Zou, C. Voon, S. Lim, X. Wu, Review of laser powder bed fusion (LPBF) fabricated Ti-6Al-4V: process, post-process treatment, microstructure, and property, *Light Adv. Manuf.* 2 (2021) 20, <https://doi.org/10.37188/lam.2021.020>
- [44] M.H. Mosallanejad, B. Niroumand, A. Aversa, A. Saboori, In-situ alloying in laser-based additive manufacturing processes: a critical review, *J. Alloy. Compd.* 872 (2021) 159567, <https://doi.org/10.1016/j.jallcom.2021.159567>
- [45] M. Simonelli, N.T. Aboulkhair, P. Cohen, J.W. Murray, A.T. Clare, C. Tuck, R.J.M. Hague, A comparison of Ti-6Al-4V in-situ alloying in selective laser melting using simply-mixed and satellited powder blend feedstocks, *Mater. Charact.* 143 (2018) 118–126, <https://doi.org/10.1016/j.matchar.2018.05.039>
- [46] M. Chen, S. Van Petegem, Z. Zou, M. Simonelli, Y.Y. Tse, C.S.T. Chang, M.G. Makowska, D. Ferreira Sanchez, H. Moens-Van Swygenhoven, Microstructural engineering of a dual-phase Ti-Al-V-Fe alloy via in situ alloying during laser powder bed fusion, *Addit. Manuf.* 59 (2022) 103173, <https://doi.org/10.1016/j.addma.2022.103173>
- [47] E.G. Brodie, A.E. Medvedev, J.E. Frith, M.S. Dargusch, H.L. Fraser, A. Molotnikov, Remelt processing and microstructure of selective laser melted Ti25Ta, *J. Alloy. Compd.* 820 (2020) 153082, <https://doi.org/10.1016/j.jallcom.2019.153082>
- [48] A. Carrozza, A. Aversa, P. Fino, M. Lombardi, Towards customized heat treatments and mechanical properties in the LPBF-processed Ti-6Al-2Sn-4Zr-6Mo alloy, *Mater. Des.* 215 (2022) 110512, <https://doi.org/10.1016/j.matdes.2022.110512>
- [49] A. Kumar, M. Sapp, J. Vincelli, M.C. Gupta, A study on laser cleaning and pulsed gas tungsten arc welding of Ti-3Al-2.5V alloy tubes, *J. Mater. Process. Technol.* 210 (1) (2010) 64–71, <https://doi.org/10.1016/j.jmatprotec.2009.08.017>
- [50] H.J. Yi, Y.J. Lee, K.O. Lee, Influences of the welding heat input and the repeated repair welding on Ti-3Al-2.5V titanium alloy, *Acta Metall. Sin. Engl. Lett.* 28 (6) (2015) 684–691, <https://doi.org/10.1007/s40195-015-0248-2>
- [51] Gunter Gottstein, *Physical Foundations of Materials Science*, 2004.
- [52] C. Leyens, M. Peters, *Titanium and Titanium Alloys*, 2003.
- [53] C. Qiu, Q. Liu, R. Ding, Significant enhancement in yield strength for a metastable beta titanium alloy by selective laser melting, *Mater. Sci. Eng. A* 816 (2021) 141291, <https://doi.org/10.1016/j.msea.2021.141291>
- [54] S. Chen, Q. Yu, The role of low angle grain boundary in deformation of titanium and its size effect, *Scr. Mater.* 163 (2019) 148–151, <https://doi.org/10.1016/j.scriptamat.2018.10.054>
- [55] G. Zhao, X.Z. Liang, B. Kim, Modelling strengthening mechanisms in beta-type Ti alloys, *Mater. Sci. Eng. A* 756 (2019) 156–160, <https://doi.org/10.1016/j.msea.2019.04.027>
- [56] M.A. Galindo-fernández, K. Mumtaz, P.E.J. Rivera-díaz-del-castillo, E.I. Galindo-nava, H. Ghadbeigi, A microstructure sensitive model for deformation of Ti-6Al-4V describing cast-and-wrought and additive manufacturing morphologies, *Mater. Des.* 160 (2018) 350–362, <https://doi.org/10.1016/j.matdes.2018.09.028>
- [57] J. He, H. Wang, H. Huang, X. Xu, M. Chen, Y. Wu, X. Liu, T.G. Nieh, K. An, Z. Lu, A precipitation-hardened high-entropy alloy with outstanding tensile properties, *Acta Mater.* 102 (2016) 187–196, <https://doi.org/10.1016/j.actamat.2015.08.076>
- [58] R. Duan, S. Li, B. Cai, W. Zhu, F. Ren, M.M. Attallah, A high strength and low modulus metastable  $\beta$  Ti-12Mo-6Zr-2Fe alloy fabricated by laser powder bed fusion in-situ alloying, *Addit. Manuf.* 37 (2021) 101708, <https://doi.org/10.1016/j.addma.2020.101708>
- [59] L. Bolzoni, E.M. Ruiz-Navas, E. Gordo, Investigation of the factors influencing the tensile behaviour of PM Ti-3Al-2.5V alloy, *Mater. Sci. Eng. A* 609 (2014) 266–272, <https://doi.org/10.1016/j.msea.2014.05.017>
- [60] J. Kwame, E. Yakushina, P. Blackwell, Influence of sheet conditions on in-plane strain evolution via ex-situ tensile deformation of Ti-3Al-2.5V at room temperature, *J. Mater. Appl.* 10 (1) (2021) 15–26, <https://doi.org/10.32732/jma.2021.10.1.15>
- [61] R. Boyer, Gerhard Welsch, E.W. Codings, *Materials Properties Handbook: Titanium Alloys*, ASM International, 1994.
- [62] S. Li, X. Lan, Z. Wang, S. Mei, Microstructure and mechanical properties of Ti-6.5Al-2Zr-Mo-V alloy processed by laser powder bed fusion and subsequent heat treatments, *Addit. Manuf.* 48 (2021) 102382, <https://doi.org/10.1016/j.addma.2021.102382>
- [63] X. Wu, D. Zhang, Y. Guo, T. Zhang, Z. Liu, Microstructure and mechanical evolution behavior of LPBF (laser powder bed fusion)-fabricated TA15 alloy, *J. Alloy. Compd.* 873 (2021) 159639, <https://doi.org/10.1016/j.jallcom.2021.159639>